

# Numerical and Experimental Assessment of Parameters Influencing the Development of Secondary Vortex Structures in Rotor Wakes

**Andrew Bodling**

Research Scientist

Science and Technology Corporation  
Moffett Field, CA, USA

**C. Christian Wolf**

Research Scientist

German Aerospace Center (DLR)  
Göttingen, Germany

**Clemens Schwarz**

Research Scientist

German Aerospace Center (DLR)  
Göttingen, Germany

**Anthony D. Gardner**

Research Scientist

German Aerospace Center (DLR)  
Göttingen, Germany

## ABSTRACT

A common phenomenon in modern high-fidelity CFD simulations is the breakdown of the primary vortex system in hover due to secondary vortex braids. In the current work, the development of secondary vortex structures in the wake of a two-bladed rotor was investigated by combining stereoscopic particle image velocimetry measurements in different measurement planes and high-fidelity simulations. Various numerical inputs including sub-iteration convergence, rotor thrust, blade pitch offset, and grid-resolution, were varied to resolve discrepancies between the measured and predicted vortex characteristics from a previous study done by the authors. A parametric study on near- and off-body solver sub-iteration convergence demonstrated that although the secondary vortex characteristics converged as the sub-iteration convergence of both solvers increased, a large discrepancy in the number of secondary vortices remained. This discrepancy was investigated by varying the thrust, where it was found that the breakdown of the primary vortex is directly linked to the number of secondary vortices. Dissimilarities in the blade pitch angle, which could not be avoided in the experiment, were modeled by intentionally using an offset in the blade pitch angle of the two blades. It was shown that as blade pitch angle offset increases, vortex pairing becomes more distinct. When vortex pairing occurred in both the experiment and simulation, the decay of secondary vortices in the experiment and simulation agreed best. To better match the experimental resolution, grid resolution was increased from 5% chord to 3% chord and comparing the two grid resolution simulations, the finer mesh simulation agreed best with the measured primary and secondary vortex characteristics.

## NOTATION

|                     |   |                         |  |
|---------------------|---|-------------------------|--|
| $c$                 | Blade chord length, $c = 0.061\text{ m}$  | $t$                     | Time (s)   |
| $c_{\text{tip}}$    | Chord length at the blade tip (m)   | $T$                     | Rotor thrust (N)   |
| $C_T$               | Thrust coefficient, $C_T = T/(\rho\pi\Omega^2 R^4)$                                   | $u, v, w$               | Velocities in $x, y, z$ direction (m/s)                                    |
| $f$                 | Focal length (m)  | $V_h$                   | Hover-induced velocity, $V_h = V_{\text{tip}}\sqrt{\frac{C_T}{2}}$ (m/s)   |
| $k$                 | Normalized turbulent kinetic energy   | $V_{\text{tip}}$        | Rotor tip speed, $V_{\text{tip}} = \Omega R = 101.76\text{ m/s}$           |
| $k_x, k_y, k_z$     | Cartesian components of $k$ , Eq. ??  | $V_{xyz}$               | Absolute velocity magnitude  |
| $k_{yz}$            | Component of $k$ in the $y, z$ -plane, Eq. ??   | $V_{yz}$                | Velocity in the $y, z$ -plane  |
| $n_{v,\text{mean}}$ | Mean vortex number per sample and $360^\circ$   | $V_\Theta$              | Swirl velocity around vortex center (m/s)                                  |
| $N_b$               | Number of blades, $N_b = 4$   | $V_{\Theta,\text{max}}$ | Maximum swirl velocity (m/s)   |
| $Q$                 | $Q$ -criterion, Eq. 1 ( $1/\text{s}^2$ )  | $x, y, z$               | Coordinates in the reference frame (m)                                     |
| $Q_s$               | Signed $Q$ -criterion, $Q_s = Q \cdot \frac{\omega_z}{ \omega_z }$ ( $1/\text{s}^2$ ) | $\Gamma$                | Circulation ( $\text{m}^2/\text{s}$ )                                      |
| $r$                 | Radial coordinate (m)   | $\Gamma_v$              | Vortex circulation at large distances ( $\text{m}^2/\text{s}$ )            |
| $r_c$               | Vortex core radius (m)  | $\lambda$               | Signed swirling strength (1/s)   |
| $R$                 | Rotor radius, $R = 0.775\text{ m}$  | $\lambda_2$             | Eigenvalues of the velocity gradient tensor $\lambda_2$ ( $1/\text{s}^2$ ) |
| $\text{Re}_v$       | Vortex Reynolds number, $\text{Re}_v = \Gamma_v/v$                                    | $v$                     | Kinematic viscosity ( $\text{m}^2/\text{s}$ )                              |
|                     |   | $\rho$                  | Air density ( $\text{kg}/\text{m}^3$ )                                     |
|                     |   | $\sigma$                | Rotor solidity, $\sigma = N_b c / \pi R = 0.05$                            |
|                     |   | $\psi$                  | Wake age ( $^\circ$ )  |
|                     |   | $\omega$                | Vorticity ( $1/\text{s}$ )   |
|                     |   | $\omega_z$              | Vorticity normal to $x, y$ -plane ( $1/\text{s}$ )                         |
|                     |   | $\Omega$                | Angular velocity of the rotor, $\Omega = 131.3\text{ rad/s}$               |

Presented at the VFS International 79th Annual Forum & Technology Display, West Palm Beach, FL, USA, May 16–18, 2023. This material is declared a work of the U.S. Government and is not subject to copyright protection in the U.S. DISTRIBUTION STATEMENT A – “Approved for public release; distribution is unlimited.” PR20230182

## INTRODUCTION

The understanding of the complex spatio-temporal development of rotor flows is still a major challenge for both state-of-the-art experimental and numerical techniques, with recent studies focusing on the phenomenon of wake breakdown and its effect on the rotor performance. An issue raised by recent high-fidelity CFD simulations is the role of secondary vortex structures in the collapse of the blade tip vortex system. Such smaller secondary vortex braids spanning between the blade tip vortices, termed “worms”, were first observed by Chaderjian and Buning (Ref. 1) and are shown in Fig. 1. These structures became a frequently observed phenomenon in simulations as high-order methods and finer grids became the state-of-the-art (Refs. 2,3). The appearance of these structures triggered a discussion whether they are an actual physical phenomenon or a purely numerical artifact connected to an insufficient convergence in the simulations (see, for example, (Refs. 4,5)). Secondary vortices impinging on structures below the rotor may impact acoustic and vibration predictions. Therefore, it is important to understand how to consistently and accurately predict their presence.

The current authors provided the first conclusive experimental proof for the occurrence of secondary vortices in the wake of a two-bladed and highly loaded model helicopter operated in ground effect (Ref. 6). The tests were conducted using the “Shake-the-Box”-method, which is a time-resolved and volumetric variant of particle image velocimetry. Later, Bodling and Potsdam (Ref. 7) performed a detailed CREATE™-AV Helios CFD study of this test case, particularly focusing on the grid and sub-iteration convergence of the Spalart-Allmaras delayed detached eddy simulation (SA-DDES). A parametric sweep on near-body sub-iterations showed that as the sub-iteration residual drop increases, the vortex sheet is broken down less and correspondingly, both the rotor performance data and peak number of secondary vortices converge. When the sub-iteration convergence or grid resolution is not high enough, the vortex sheet and primary vortex are broken down, which disrupts the development process and leads to fewer secondary vortices. A simplified vortex ring study was performed to observe how vortex breakdown is influenced by off-body grid structure and different levels of sub-iteration convergence. In agreement with the rotor case, when all flow solvers were sufficiently converged, vortex breakdown was minimized. Using a case with a relatively high sub-iteration convergence and grid resolution, the measurements and predictions showed good qualitative agreement, which included several similarities such as a mix of positive and negative secondary vortices, the width of the vortices, and the evolution of the vortices over time. However, despite the good qualitative agreement between the experimental data and the simulations, the degree to which the simulations were predicting the correct number of secondary vortices was still in question due to the lack of quantitative comparisons made. The lack of quantitative data was mainly due to the experimental restrictions

imposed by the novel volumetric measurements. The achievable tracer particle density using helium-filled soap bubbles and thus the spatial resolution of the measurements was limited, possibly hampering the detection of small-scale vortex structures. Direct comparisons to the data were also complicated by uncertainties related to the experimental setup. For example, for a given rotor wake age, the measured secondary vortices would greatly vary depending on the rotor cycle. The pronounced cycle-to-cycle aperiodicity of the wake was triggered by the test enclosure, the asymmetric helicopter fuselage and tail rotor, etc.

Therefore, a joint experimental-numerical effort with an improved setup was later launched (Ref. 8). To reduce the cycle to cycle variations, the same model rotor was incorporated into a new rotor test bed enabling out-of-ground-effect operation with a symmetric support structure and a high-speed stereoscopic PIV system that provided a higher spatial resolution compared to the previous “Shake-The-Box” measurements. Simultaneously, a high-fidelity simulation with Helios was conducted. Both qualitative and quantitative experimental corroboration with computation of the existence, strength, and number of secondary vortices was shown. This study also gave a greater understanding of the secondary vortices development, behavior, stability and decay.

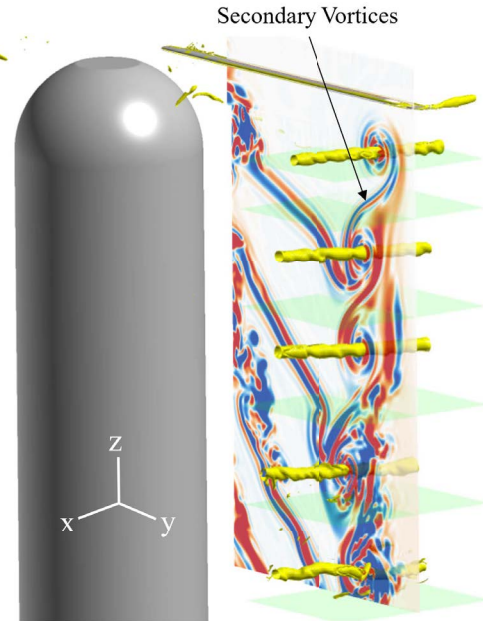


Figure 1: Visualization of wake vortex system.

Although the predicted and measured vortex characteristics agreed well in Schwarz et al. (Ref. 8), there were some discrepancies between the experiment and simulation, and it was not clear what sources of error were causing these discrepancies. The goal of this study is to build on the previous investigation by Schwarz et al. (Ref. 8) and identify the sources of error that are causing the discrepancies. The numerical inputs are varied to progressively increase the accuracy of the predicted primary and secondary vortex characteristics. We will investigate how well the predictions agree with the measure-

ments once sub-iteration convergence is high enough. The relation between tip vortex breakdown and the number of secondary vortices will be shown. Additionally, this study will investigate what role vortex pairing has on the decay of the secondary vortices. Finally, the grid resolution is increased to observe how the predictions are affected as the simulation approaches the experimental resolution. Using the numerical setup that best agrees with the experiment, the solution will then be used to elucidate the development and decay of the secondary vortices.

## EXPERIMENTAL AND NUMERICAL SETUP

### Test rotor

The two-bladed test rotor has a rotor radius of  $R = 0.775$  m and is operated in a laser laboratory at the German Aerospace Center (DLR) in Göttingen, Germany. The room has a dimension of about  $10\text{ m} \times 12\text{ m} \times 7\text{ m}$ . The rotor is mounted on a rigid support structure with a height of  $4R$  above the ground to avoid ground effect. It is equipped with two un-twisted and untapered “Spinblades Black Belt 685” rotor blades with a chord length of  $c = 0.061$  m. They have a parabolic tip and a symmetrical airfoil with a thickness-to-chord ratio of 14.8%. The rotational frequency of the rotor is set to  $\Omega = 131.3\text{ rad/s}$  or 20.9 Hz. The blade pitch is set to  $10.4^\circ$ , corresponding to a rotor thrust of 112.8 N, which is measured with a piezoelectric balance. This corresponds to approximately 80% of the rotor’s maximum thrust and was chosen to achieve similar loading conditions as in the investigation by Wolf et al. (Ref. 6). This results in a thrust coefficient of  $C_T = T/\rho\pi\Omega^2 R^4 = 0.0048$  with the air density  $\rho = 1.20\text{ kg/m}^3$ , and in a blade loading of  $C_T/\sigma = 0.096$ . The induced velocity in hover equates to  $V_h = 4.98\text{ m/s}$ .

### Particle image velocimetry

The flow field below the rotor is studied using time-resolved stereoscopic particle image velocimetry (PIV) with an acquisition frequency of 945 double images per second or 45 images per rotor revolution. A high-speed laser with an energy output of 26 mJ/pulse and a time delay of  $\Delta t = 50\mu\text{s}$  between two pulses is used. The laser beam is expanded into a light sheet which is vertically traversed over the course of the experiment to illuminate the flow at different heights below the rotor plane. A total of 7 horizontal measurement domains ranging from  $z = -0.1R$  to  $z = -1.2R$  below the rotor plane are investigated successively. The setup with the indicated horizontal field of views (FOVs) is depicted in Fig. 2. In addition, two vertically oriented measurement planes which are stacked on top of each other are used to capture a large portion of the wake including the blade tip vortices. An encoder enables a phase-locked triggering of the measurements. The entire test facility is densely seeded with droplets of di-ethyl-hexyl-sebacate (DEHS) of 1.2 to  $2.3\text{ }\mu\text{m}$  particle size. Both PIV cameras (Phantom VEO640L, see (Ref. 8)) are operated with a reduced resolution of  $2176 \times 1452$  pixels and equipped

with lenses with a focal length of 180 mm for the horizontal FOVs and 85 mm for the vertically oriented overview measurement planes.

### Hot-wire anemometry

Hot-wire measurements were performed complementary to the PIV investigation to allow for the determination of turbulence parameters. The hot-wire probe was a single sensor probe by TSI, type “1210-T1.5”, and was operated with a “DISA 55M” anemometer unit consisting of a standard bridge and an amplifier. The probe was operated using the constant temperature anemometry (CTA) measurement principle in which the probe is heated up to a significantly higher temperature than the investigated fluid. With the use of a fast controlling unit, the hot-wire’s resistance and thus the temperature is kept constant. The heat transfer due to convection is in turn represented by the measured voltage and is used to determine the air speed. With the low inertia of this system, high frequencies can be measured. The data was recorded at a sampling rate of 200 kHz. The response time of the hot-wire probe was around  $8\mu\text{s}$ , which leads to a theoretical bandwidth of 100 kHz. The probe was oriented parallel to the  $x$ -axis and thus measured the absolute value of the instantaneous velocity component in the  $y,z$ -plane. Measurements were taken at 7 radial positions in the wake ranging from  $y/R = 0.7$  to  $y/R = 1.0$  and at 34 axial locations. In the axial direction, the wake was spatially sampled in steps of 25 mm, resulting in a normalized range of  $z/R = -0.0645$  to  $z/R = -1.129$ .

## NUMERICAL SETUP

### Numerical Methodology

For the simulations, Helios version 12.2 (Ref. 9) is used. Helios is the rotary-wing product of the US Army and HPCMP CREATE™-AV (Air Vehicles) program sponsored by the DoD High Performance Computing Modernization Office. Helios employs an innovative multi-mesh, multi-solver paradigm for computational fluid dynamics (CFD) that uses unstructured and/or structured meshes in the “near-body” surrounding the solid surfaces to capture the wall-bounded viscous effects. Several near-body solvers are available in the latest Helios release, including unstructured mesh FUN3D, and kCFD; curvilinear structured mesh OVERFLOW; and strand mesh mStrand. Cartesian grids are used in the “off-body” to resolve the wake through a combination of high-order algorithms and adaptive mesh refinement (AMR). The Cartesian meshes are managed by a block structured mesh system which has the ability to accommodate the geometry and solution features. An overset procedure (PUNDIT) (Ref. 10) facilitates the data exchange and also enables the relative motion between moving meshes. A lightweight Python-based software integration framework orchestrates the simulation and data exchange between modules.

The main Helios flow solver modules used in this study are described in the following sections.

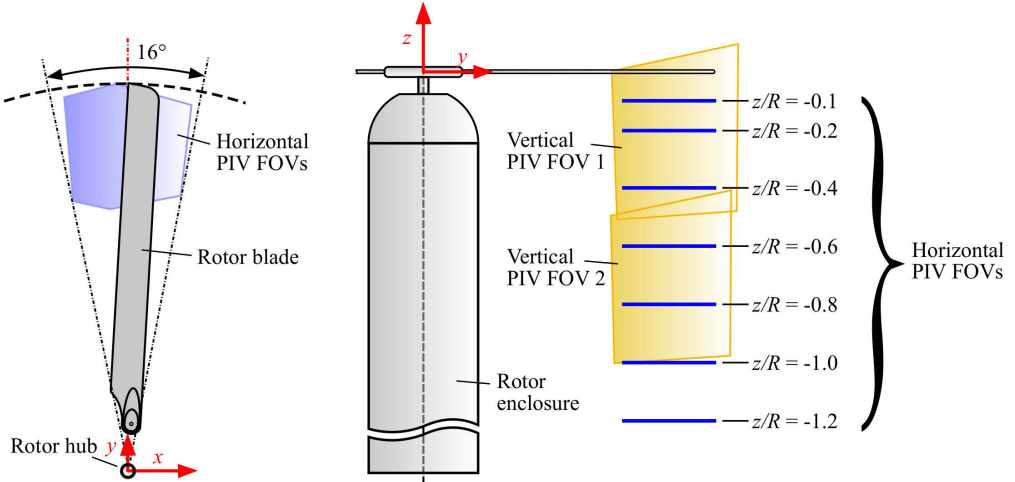


Figure 2: Sketch of rotor setup and PIV fields of view (FOV).

## Flow Solvers

### FUN3D

FUN3D 13.5 (Ref. 11) is a near-body unstructured grid flow solver that has been continuously developed and supported by NASA Langley. It is a node-centered, finite-volume unsteady Reynolds-Averaged Navier-Stokes (URANS) solver. It is spatially 2nd-order accurate using a Roe upwind scheme. Time-accurate computations utilize an optimized, second-order, backward difference (BDF2OPT) time stepping scheme along with dual-time stepping sub-iterations. The SA-DDES turbulence model with Dacles-Mariani rotation correction and negative turbulence variable provisions are used (Refs. 12–14).

### OVERFLOW

The near-body solver OVERFLOW 2.3b (Ref. 15), a structured, curvilinear grid flow solver developed by NASA Langley, is a node-centered, finite-difference unsteady Reynolds-Averaged Navier-Stokes (URANS) solver. A nominally spatially sixth-order accurate central difference scheme with sixth-difference-based scalar artificial dissipation is chosen for this study. The amount of artificial dissipation is controlled by the dissipation coefficient DIS4 and the smoothing parameter SMOO which changes how the spectral radius of the Jacobian matrix is computed. Based on previous numerical experiments, a value of DIS4 between 0.005 and 0.04 is recommended, where the DIS4 coefficient used should be kept as small as possible while still maintaining stability. With SMOO = 0.0, the spectral radius is computed as normally,  $|U| + kc$ . With SMOO = 1.0, the sound speed  $c$  is replaced by the local velocity scaled by the reference Mach number  $\|V\|/M_{ref}$ , which reduces smoothing in low-speed regions. Intermediate values of SMOO combine the effects of both the speed of sound and local velocity. More information about these parameters, including the form of the artificial dissipation operator is given in Jespersen et

al. (Ref. 16). Time-accurate computations utilize an optimized, second-order, backward difference (BDF2OPT) time stepping scheme along with dual-time stepping sub-iterations. The SA-DDES turbulence model with Dacles-Mariani rotation correction is used (Ref. 17).

### SAMCart

The Cartesian solver SAMCart is used for the off-body mesh system (Refs. 18, 19). SAMCart solves the Euler or Navier-Stokes equations using a 5th-order accurate central difference spatial discretization scheme for the inviscid terms and 4th-order for the viscous terms. The solver uses an implicit 2nd-order BDF2 LU-SGS time integration scheme. AMR can be used to accurately, efficiently and automatically capture the features in unsteady flow based on suitable adaption criteria. User-defined rectangular regions of a particular grid resolution can also be input. This fixed refinement capability is used in the current effort in order to fully and uniformly capture the blade wake sheets and tip vortices. The SA-DES turbulence model with Dacles-Mariani rotation correction is used.

### Geometry Modeling, Meshing, and Boundary Conditions

The boundary conditions at the cylinder hub and rotor blades are viscous adiabatic solid walls (i.e. no slip wall with density/pressure extrapolation). Free stream conditions are used at the farfield boundaries with an inviscid ground plane  $4R$  below the rotor. The farfield boundaries are  $15R$  away from the blades in each direction to avoid any boundary effects on the nearfield solution. The experiment includes a small amount of blade bending and coning, which the calculations do not account for. Since the cylinder hub should be sufficient to capture hub blockage effects, the rotor geometry was cut off at  $0.20R$  and the remaining components such as the blade attachments and pitch links have been ignored.

Figure 3 shows a top and side view of the computational meshes. The red boundaries denote the no slip walls of

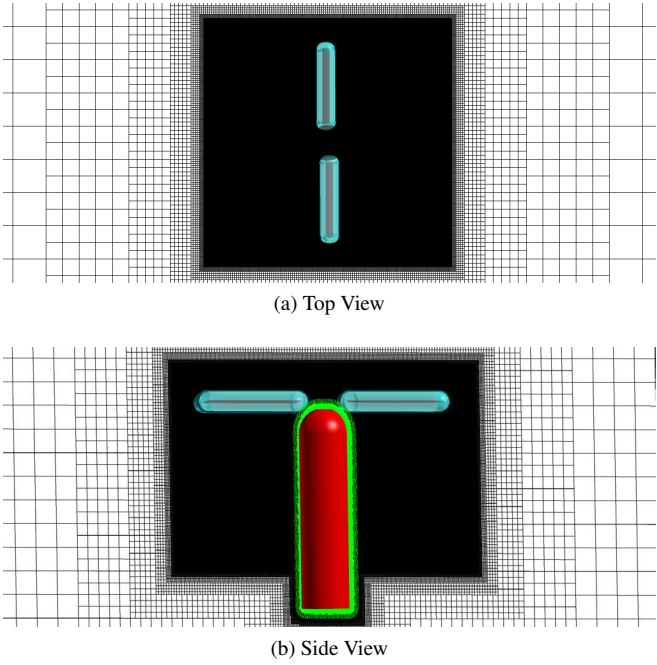


Figure 3: Top and side views of the computational meshes.

Table 1: Number of Grid Points for Main Mesh Components (without fringes)

| Volume Mesh               | Number of Grid Points |
|---------------------------|-----------------------|
| Coarse Cylinder Hub       | 1.9M                  |
| Fine Cylinder Hub         | 3.6M                  |
| Coarse Total Blade        | 10.6M                 |
| Fine Total Blade          | 27.5M                 |
| Coarse Main Blade         | 7.6M                  |
| Fine Main Blade           | 22.4M                 |
| Coarse Cartesian Off-body | 0.635B                |
| Fine Cartesian Off-body   | 1.46B                 |

the cylinder hub and blades. The green mesh indicates the trimmed unstructured near-body mesh used to model the cylinder hub, which is solved by FUN3D. Throughout the entire cylinder grid,  $y^+ < 1$ . All FUN3D calculations use 10 sub-iterations, which ensures a 3 orders of magnitude (OOM) sub-iteration residual drop or an absolute residual of 10 OOM at the final sub-iteration. The residual drop is computed from the  $L_2$ -norm of the mean flow residual and is not volume-scaled. The cyan mesh is the extents of the structured volume mesh that is used to model the rotor blades and is solved by OVERFLOW. The rotor blade grids consists of overlapping main blade, root cap, and tip cap meshes. Each blade, root cap and tip cap mesh extends out 1.1 chords. The black mesh denotes the off-body Cartesian mesh that is solved by SAM-Cart.

The wake is resolved with a single fixed refinement box. The resolution of this fixed refinement box is varied in this paper to investigate the effects of grid resolution. A grid resolution of  $\Delta x = \Delta y = \Delta z = 5\% c_{tip} = 0.0021$  m and  $\Delta x = \Delta y = \Delta z = 3\% c_{tip} = 0.00126$  m is used, where  $c_{tip}$  is the airfoil chord

at the blade tip. The  $5\% c$  resolution simulations extend to  $z/R = -1.25$ . Due to solver constraints, the  $3\% c$  resolution simulations extend to  $z/R = -1.0$ . Outside the fixed refinement box, the mesh is progressively coarsened by a factor of two in all directions. A summary of the number of grid points for the main mesh components is shown in Table 1, where “coarse” and “fine” refers to the simulations using an off-body fixed refinement box mesh spacing of  $5\% c$  and  $3\% c$ , respectively. The chordwise  $x$  spanwise  $x$  normal dimensions of the “coarse” and “fine” mesh blade is 311 x 241 x 101 and 423 x 352 x 151 points, respectively. To ensure high quality overset between the near and off-body grids, the outer boundary mesh spacing of the near-body volume meshes for the “coarse” and “fine” simulations is the same spacing as the respective off-body grid ( $5\% c$  and  $3\% c$ ). All cases presented in this manuscript are run with a time-step size of  $\Delta t = 0.25^\circ$ .

## RESULTS

We start by using the numerical inputs used in the previous study done by Schwarz et al. (Ref. 8) with a fixed refinement box resolution of  $\Delta x = \Delta y = \Delta z = 5\% c_{tip} = 0.0021$  m, high numerical dissipation (0.04 artificial dissipation coefficient and 0.0 smoothing parameter), a blade pitch angle of  $\beta = 10.4^\circ$ , 50 near-body (OVERFLOW) sub-iterations and 10 off-body (SAMCart) sub-iterations. Each case shown in this manuscript is run sufficiently long to let any initial start-up transients to die out. After 10 revolutions, the figure of merit for each case changed less than 0.1%. All snapshots and time-averaging shown are after 16 revolutions, which is several revolutions after the integrated forces have become statistically stationary.

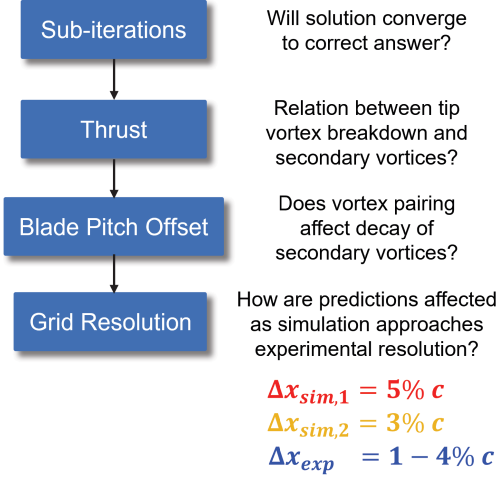


Figure 4: Outline of primary and secondary vortex analysis

Figure 4 shows an outline of the primary and secondary vortex analysis. We will first vary sub-iterations to see if the solution converges to the correct answer. Then the rotor thrust is varied to determine the relationship between the breakdown of the tip vortices and the secondary vortices. Next the blade pitch offset is varied to see if vortex pairing affects the decay of the secondary vortices. In the experiment, the grid resolution is

approximately 1 to 4% of the chord, where 1% is the vector spacing and 4% is the interrogation window size. The grid resolution of the simulations will be increased from 5% $c$  to 3% $c$  to see how the predictions are affected as the simulation approaches the range of the experimental resolution. Using the numerical setup that best agrees with the experiment, the solution will then be used to elucidate the development and decay of the secondary vortices.

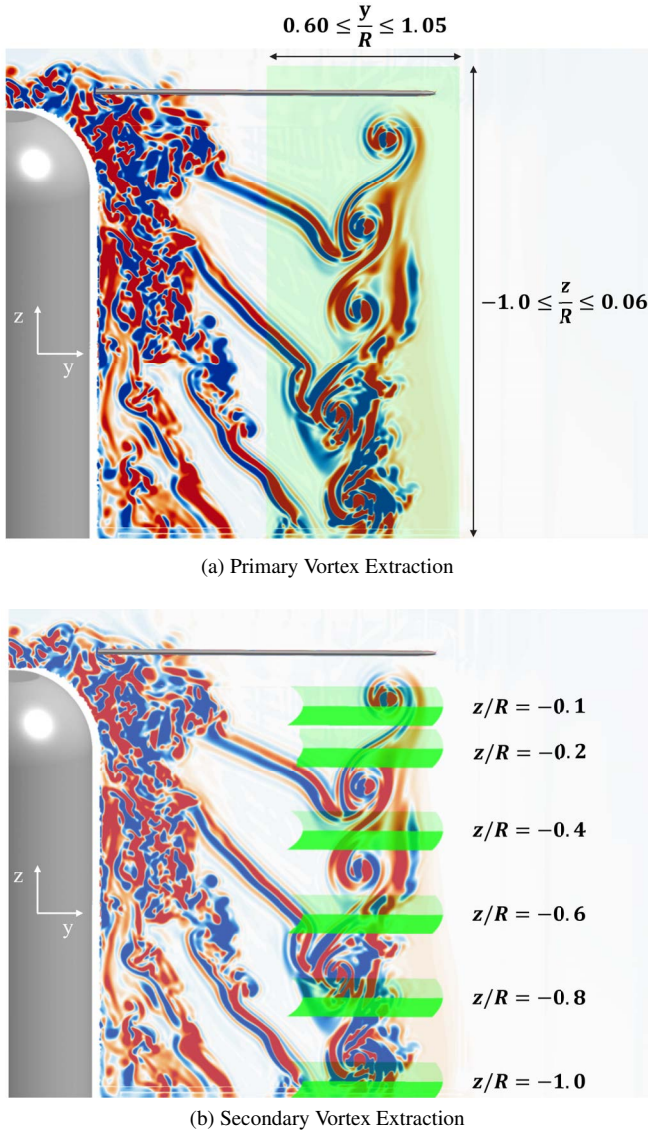


Figure 5: Primary (top) and secondary (bottom) vortex data extraction

In both the experiment and simulation, a vertical plane is extracted to characterize the primary vortices. This plane, which extends one radius below the radius, is illustrated in Fig 5 (a). Also in both the experiment and simulation, horizontal planes are extracted to characterize the secondary vortices. As shown in Fig 5 (b), these planes extend from 0.1 to 1 radius below the rotor and in the radial direction from  $r = 0.68R$  to  $r = 1.01R$ . The number of secondary vortices at each axial position is quantified using the vortex identification scheme

from Schwarz et al. (Ref. 8). For a given horizontal slice, the  $Q$ -criterion is applied to the velocity fields.  $Q$  is derived based on the assumption of a 2D velocity gradient tensor from the in-plane velocity components ( $u, v$ ) according to Chen et al. (Ref. 20) by

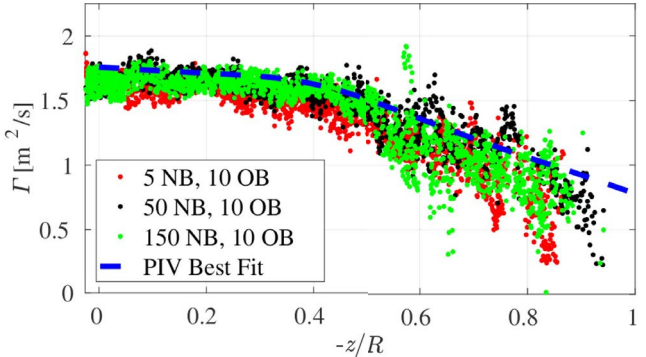
$$Q = \frac{\partial u}{\partial x} \frac{\partial v}{\partial y} - \frac{\partial u}{\partial y} \frac{\partial v}{\partial x} - \frac{1}{2} \left( \frac{\partial u}{\partial x} + \frac{\partial v}{\partial y} \right)^2. \quad (1)$$

The  $Q$ -values are calculated based on velocity fields that are postprocessed using a 2D median filter (filter that replaces each entry with the median of the neighboring entries) with a size of 5.04 mm ( $= 4\Delta x = 4\Delta y$ ) in both spatial directions to suppress noise. Only areas exceeding a threshold of  $Q = 0.10$  are accepted while all lower values are set to zero. Additionally, the “bwpropfilt” function in MATLAB is used to only accept connected areas exceeding the  $Q$ -threshold that feature a minimum minor axis length of 4.12 mm. The minor axis length specifies the length of the minor axis of the ellipse that has the same normalized second central moments as the region. The  $Q$ -threshold, median filter size and minimum minor axis length are identical for post processing the experimental and simulation data. These values were fine-tuned based off of how much noise was observed in the detected secondary vortices. This approach was used in the joint experimental and numerical investigation from Schwarz et al. (Ref. 8) to quantify the development of secondary vortex structures in the wake of a two-bladed rotor out of ground effect. In that study, the number of secondary vortices detected in the experiment and simulation agreed well for axial positions  $z/R \geq -0.6$ . For this analysis, data is sampled every four time-steps (or every  $1^\circ$ ) over a duration of five revolutions, resulting in 1800 velocity fields at each axial station. For a given axial position, the number of secondary vortices in the horizontal plane is computed at each time-step. Then the average number of secondary vortices per time-step for each axial position is found. For the experiment and simulations, for each horizontal plane, the average detected number of secondary vortices per time step is extrapolated to  $360^\circ$  azimuth.

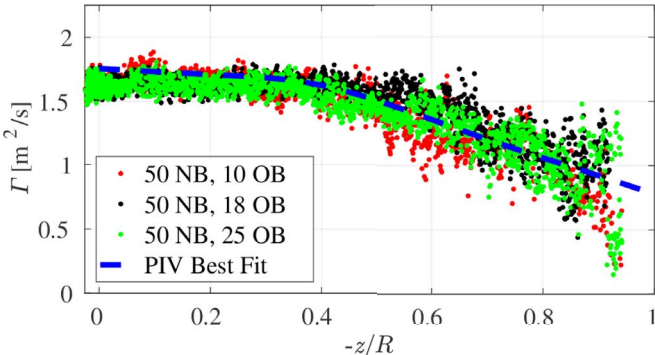
### Effect of Sub-iteration Convergence

Figures 6 and 7 shows the measured and predicted phase-averaged primary vortex characteristics, circulation  $\Gamma$  and max swirl velocity  $V_{\theta,\max}/V_h$ , as the near-body (NB) and off-body (OB) solver sub-iterations increase. 5, 50 and 150 NB sub-iterations are used, which corresponds to an average global residual drop of 0.75, 1.52, and 2.08 OOM, respectively; OB sub-iterations are increased from 10 to 18 to 25, which corresponds to an average global residual drop of 1.1, 2.1 and 2.8 OOM, respectively. For clarity, only the best fit line of the phase-averaged PIV data is shown. Besides the slight increase in max swirl velocity  $V_{\theta,\max}/V_h$  as off-body sub-iterations increase, the primary vortex characteristics do not change significantly as the sub-iteration convergence (or sub-iterations) of both solvers increase.

Figure 8 shows a comparison of the predicted and measured average number of secondary vortices per time-step along



(a) Increase near-body (NB) sub-iterations



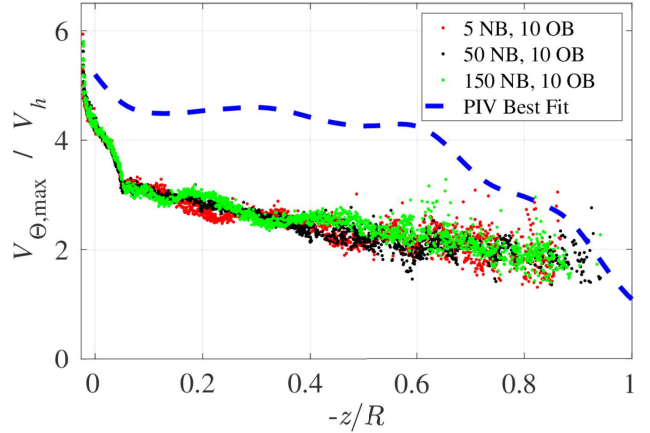
(b) Increase off-body (OB) sub-iterations

Figure 6: Effect of increasing near-body (NB) and off-body (OB) sub-iterations on primary vortex circulation with the 5% $c$  simulation.

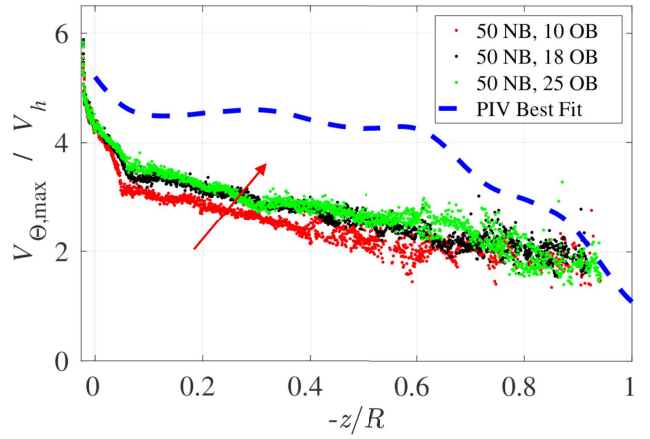
the axial direction for the parametric sweep on NB and OB sub-iterations. As the sub-iteration convergence of both flow solvers increases, the number of secondary vortices converge. However, comparing the measured and predicted data, a large discrepancy remains for  $z/R < -0.6$ . This suggests there is another source of error that is causing the discrepancy in the number of secondary vortices. One hypothesis for what is causing the discrepancy is that there is a relation between the breakdown of the tip vortex and the number of secondary vortices and therefore, if the predictions are not accurately capturing the breakdown of the tip vortex, this would lead to the discrepancy in the number of secondary vortices. In the ensuing section, the rotor thrust is varied to better understand this hypothesis.

### Effect of Rotor Thrust

Figure 9 shows the predicted tip vortex breakdown for the three thrust levels, visualized via Q-criterion ( $Q = 8.65$ ). Iso-surfaces with a x-vorticity  $\omega_x U_\infty / c$  outside the range of 3 to 30 have been filtered out, where  $x$  is in the longitudinal direction of the tip vortex. Comparing the three thrust levels, the primary vortex breaks down more with lower thrust. Figure 10 shows the phase-averaged tip vortex circulation as thrust is varied. The circulation plot shows that the tip vortex circulation drops off more with lower thrust. Comparing the trends in Figs. 9 and Fig. 10, these results suggests that observing a



(a) Increase NB sub-iterations



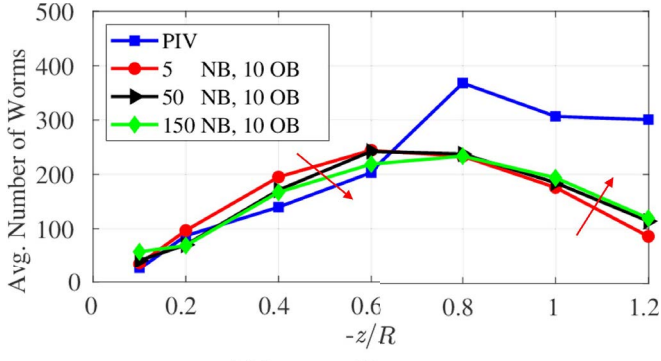
(b) Increase OB sub-iterations

Figure 7: Effect of increasing NB and OB sub-iterations on primary vortex maximum swirl velocity  $V_{\theta,\max} / V_h$  with the 5% $c$  simulation.

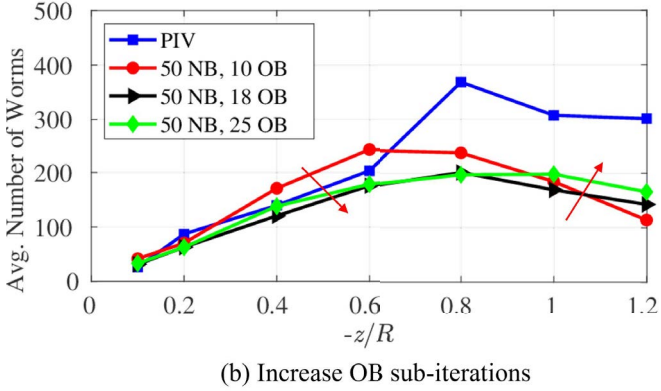
drop in tip vortex circulation could be associated with a more broken down tip vortex. This conclusion is important for understanding a discrepancy observed later in the manuscript. Figure 11 shows a visualization of the breakdown of the tip vortex and the corresponding variation in secondary vortices for the three thrust levels; figure 12 shows the computed number of secondary vortices as thrust is varied. In the most downstream portion of the flow (denoted by the red box), a more broken down primary vortex correlates with fewer secondary vortices. Therefore, this demonstrates that breakdown of the primary vortex is directly linked to the number of secondary vortices. Since vortex pairing (observed in Schwarz et al. (Ref. 8)) occurs in the experiment but not the simulation, this could explain the discrepancy in the number of secondary vortices in the previous section. The reason for why vortex pairing occurs in the experiment but not the simulation is investigated with blade pitch angle offset in the next section.

### Effect of Blade Pitch Angle Offset

In the experiment, ideally the blade pitch angle of the two blades is trimmed to the same exact blade pitch angle. How-



(a) Increase NB sub-iterations



(b) Increase OB sub-iterations

Figure 8: Effect of increasing NB and OB sub-iterations on average number of secondary vortices. For the experiment and simulations, for each horizontal plane, the average detected number of secondary vortices per time step is extrapolated to  $360^\circ$  azimuth.

ever, measurement uncertainties and differences in the blades elastic behavior may lead to slight offsets in the blade pitch angle between the two blades. This section will model this uncertainty by intentionally using an offset in the blade pitch angle of the two blades to see if the offset can lead to vortex pairing in the simulation; the predicted and measured number of secondary vortices is compared to see if the predictions match better with the measurements if vortex pairing occurs. A blade pitch angle offset of  $0.0^\circ$ ,  $0.1^\circ$ , and  $0.5^\circ$  is used. Generally, with lower numerical dissipation, the solution is more accurate as long as it remains stable. Therefore, for all three cases, as well as the remainder of the manuscript, the artificial dissipation coefficient is decreased from 0.04 to 0.01, which slightly decreases the number of secondary vortices for  $z/R \geq -0.8$  (not shown). Also, for the  $0.0^\circ$  offset case, the blade pitch angle is increased to  $11.1^\circ$  to match the measured rotor thrust. The  $0.1^\circ$  and  $0.5^\circ$  offset cases use the same blade pitch angle for blade one but a blade pitch angle of  $11.2^\circ$  and  $11.6^\circ$ , respectively, for the second blade. Figure 13 shows a comparison of the vorticity magnitude contour plots for all three blade pitch angle offset cases. The contour slice is located at the  $x = 0$  plane. The phase-averaged blade tip vortex trajectory (black markers) is superimposed onto the contour plot. As shown in the plots, with no offset, there is a single vortex trajectory while with the blade pitch offset, especially with  $0.5^\circ$  offset, two distinct trajectories occur, which indicate

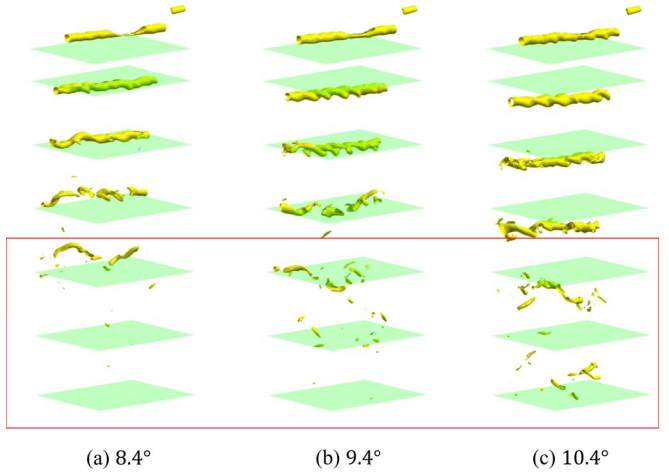


Figure 9: Predicted tip vortex breakdown for  $8.4^\circ$ ,  $9.4^\circ$  and  $10.4^\circ$  blade pitch angle, visualized via Q-criterion.

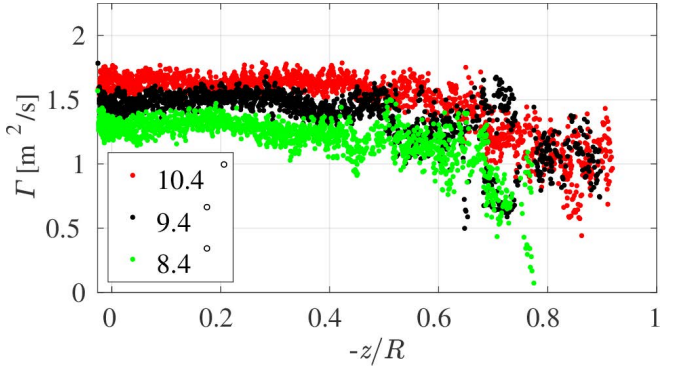


Figure 10: Predicted phase-averaged tip vortex circulation for  $8.4^\circ$ ,  $9.4^\circ$ , and  $10.4^\circ$  blade pitch angle.

the presence of vortex pairing.

Figure 14 shows how the phase-averaged tip vortex trajectory and number of secondary vortices varies as the blade pitch angle offset increases. Comparing the average number of secondary vortices, the peak value occurring at  $z/R = -0.8$  is captured in the predictions for the  $0.5^\circ$  offset case, which is the case that has the most distinct vortex pairing. This demonstrates that when vortex pairing occurs in both the experiment and simulation, the decay of secondary vortices in the experiment and simulation agree best. For  $0.5^\circ$  offset, the difference between experiment and simulation becomes more of a difference in the absolute number while the qualitative trend is captured correctly. As a reminder, the experimental resolution is between 1 and  $4\%c$  while the current simulation grid resolution is  $5\%c$ . Therefore, the absolute difference in secondary vortices could be due to insufficient grid resolution in the simulation. This is investigated in the next section by increasing the grid resolution from  $5\%c$  to  $3\%c$ .

## Effect of Grid Resolution

**Comparing Overall Wake Structure and Blade Tip Vortices** This section will seek to understand if the differences

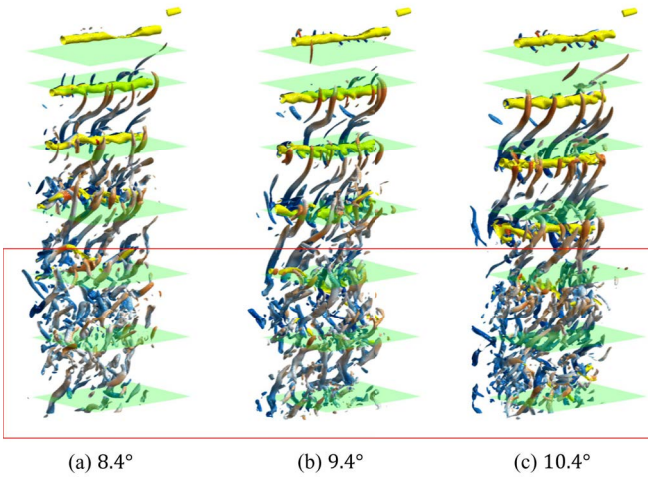


Figure 11: Predicted breakdown of tip vortex and the associated variation in secondary vortices for  $8.4^\circ$ ,  $9.4^\circ$  and  $10.4^\circ$  blade pitch angle.

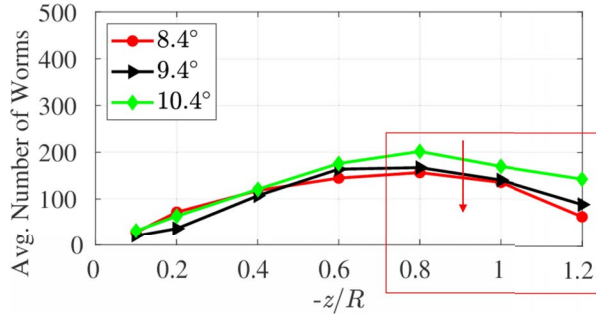


Figure 12: Figure shows variation in predicted secondary vortices as thrust is varied via blade pitch angle.

between the experiment and simulation are merely because of insufficient grid resolution. The grid resolution study will be done with a  $0.5^\circ$  blade pitch offset. A grid resolution of  $\Delta x = \Delta y = \Delta z = 5\%c_{tip} = 0.0021$  m and  $\Delta x = \Delta y = \Delta z = 3\%c_{tip} = 0.00126$  m is used.

As seen in the previous section, primary vortex evolution is important for predicting the secondary vortex development. Therefore, the overall wake structure and blade tip vortices are analyzed using  $5\%c$  and  $3\%c$  grid resolution. Figure 15 shows a comparison of velocity (a+c) and turbulent kinetic energy (TKE) (b+d) profiles along the radial direction at an axial position of  $z/R = -0.194$ . Comparing the measured and predicted profiles of the two simulations, the finer resolution mesh better predicts the velocity and kinetic energy profiles. Both the magnitude and location of peak TKE is better resolved with finer resolution. The wake profiles of the finer resolution simulation also shows better agreement with the experiment than the previously reported simulation in Schwarz et al. (Ref. 8). Figure 16 shows a comparison of the primary vortex characteristics for the experiment and the two different grid resolutions. The figure shows that swirl velocity is better predicted with finer resolution grid. However, the circulation of the coarser grid simulation better matches with the experiment. The coarser grid circulation drops off

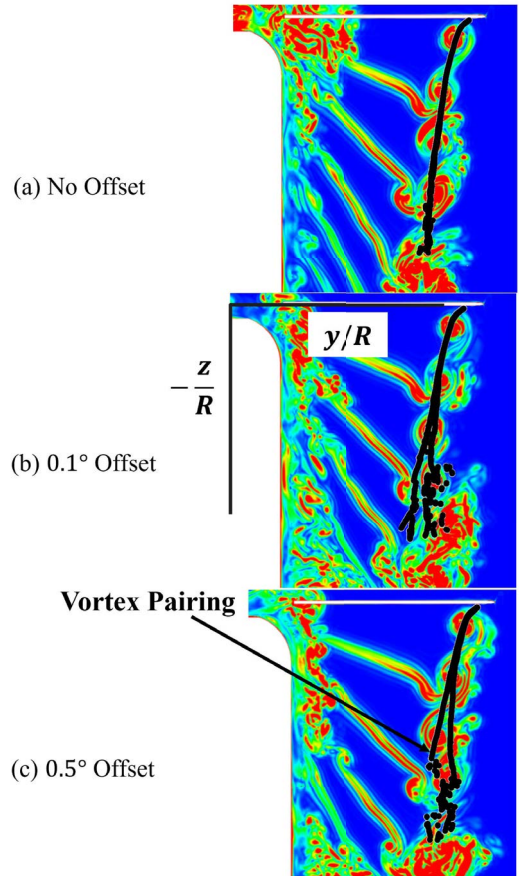
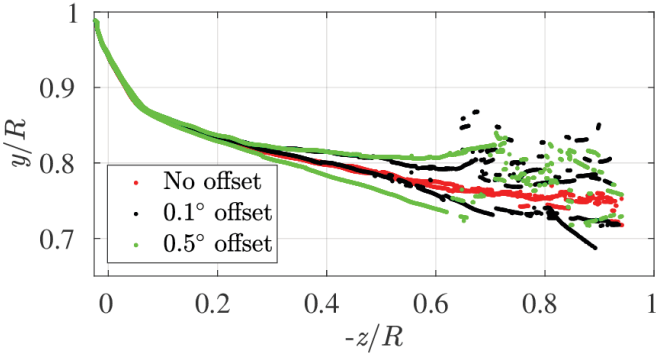


Figure 13: Effect of blade pitch angle offset on vortex pairing is shown with vorticity magnitude contour plots for a blade pitch angle offset of  $0.0^\circ$ ,  $0.1^\circ$ , and  $0.5^\circ$ . Contour slice is taken at  $x = 0$ .

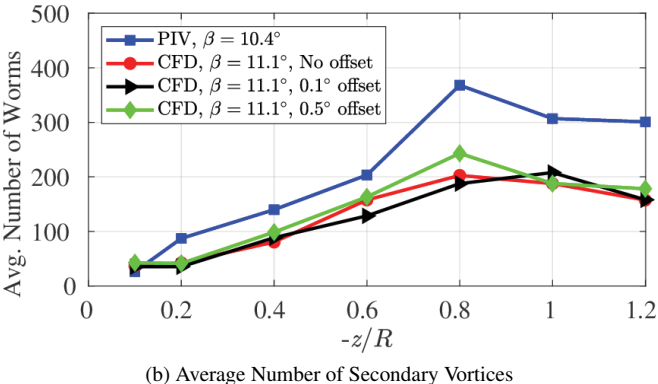
at around  $z/R = -0.6$  while the finer grid remains relatively constant. In the previous section (see Fig. 10), it was observed that the circulation dropped off as the tip vortex broke down more. Therefore, this suggests that the primary vortex breaks down sooner with the  $5\%c$  case and the experiment. More research is needed to fully understand this discrepancy.

**Comparing the Secondary Vortex Development** Figure 17 shows a comparison of the measured vs predicted ( $5\%c$  and  $3\%c$ ) sample velocity fields at wake age of  $\Psi_w = 125^\circ$  taken at a horizontal plane of  $z/R = -0.4$ . The contours represent the signed  $Q$  values after applying the filtering scheme for secondary vortex detection. The shape of the secondary vortices in the finer grid simulation better resemble the measured secondary vortices than the coarser simulation. The secondary vortices in the finer resolution simulation also shows better agreement with the experiment than the previously reported simulation in Schwarz et al. (Ref. 8).

Figure 18 shows the variation in predicted secondary vortices as grid resolution and sub-iteration convergence varies. A summary of the sub-iterations (SI) and global sub-iteration residual drop (RD) is shown in Table 2. Comparing  $5\%c$  and  $3\%c$  high sub-iteration convergence (red and orange lines),  $3\%c$  better matches the number of secondary vortices



(a) Phase-averaged Blade Tip Vortex Trajectory



(b) Average Number of Secondary Vortices

Figure 14: Effect of blade pitch angle offset on vortex pairing is shown with phase-averaged blade tip vortex trajectory profiles and the resulting average number of secondary vortices.

in the experiment. For the 3% $c$  simulation, if using lower sub-iteration convergence (black line) there is actually more secondary vortices, which agrees less with the experiment. Bodling and Potsdam (Ref. 7) showed that high sub-iteration convergence is required to minimize breakdown of the vortex sheet. These additional secondary vortices could be artifacts due to the vortex sheet being broken down more, which causes spurious secondary vortices. Interestingly, the 3% $c$  low sub-iteration convergence case and the 5% $c$  case correctly predicts the location of the peak value occurring at  $z/R = -0.8$ , while with the 3% $c$  high sub-iteration convergence case, the number of secondary vortices continues to increase past  $z/R = -0.8$ . It appears this error is related to the discrepancy in circulation observed in Fig. 16, where the primary vortex was believed to break down sooner with the 5% $c$  case than the 3% $c$  case. Higher numerical dissipation due to low sub-iteration convergence or insufficient grid resolution may artificially cause the primary vortex to break down sooner and thereby, *coincidentally* match the peak location of the experiment. This coincidence may occur if there is another source of error that is not being accounted for in the current simulations, such as inadequate turbulence modeling. The use of large eddy simulations (LES) or turbulence transition models may help shed light on this discrepancy.

To better understand the effect of grid resolution, we compare the secondary vortex histograms at  $z/R = -0.8$  for 5% $c$  and 3% $c$  grid resolution with high sub-iteration convergence

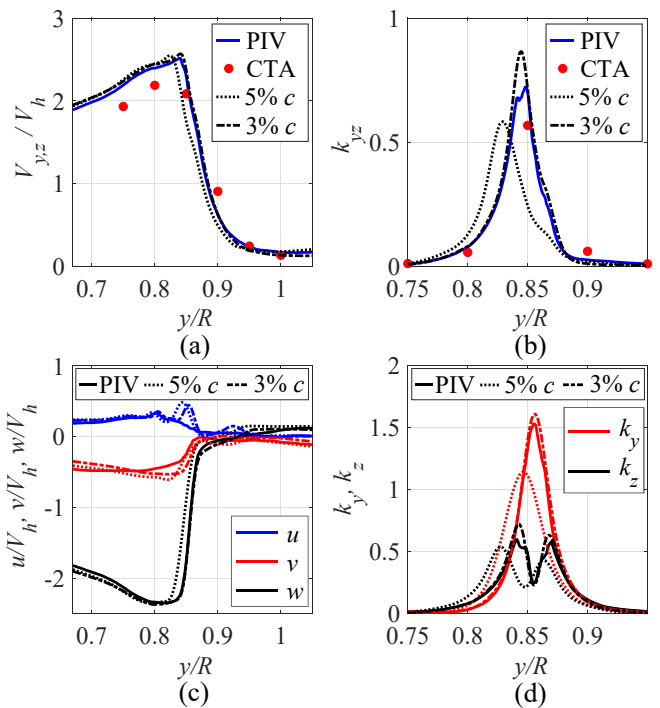
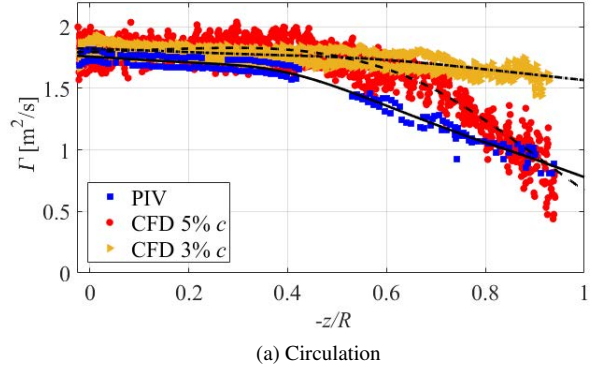
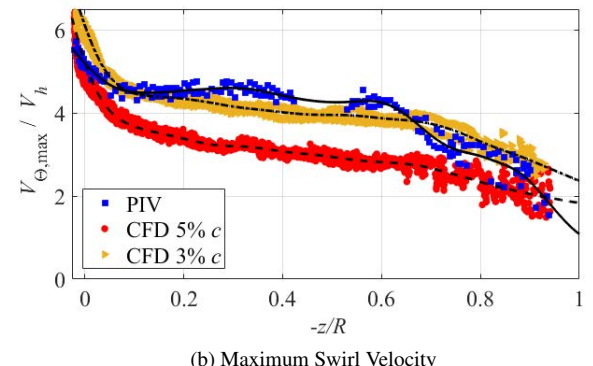


Figure 15: Comparison of velocity (a+c) and turbulent kinetic energy (TKE) (b+d) profiles along the radial direction at an axial position of  $z/R = -0.194$ . Predictions are with 0.5° blade pitch angle offset.



(a) Circulation



(b) Maximum Swirl Velocity

Figure 16: Phase-averaged blade tip vortex circulation  $\Gamma$  (a) and maximum swirl velocity  $V_{\theta,\max}/V_h$  (b) over axial position  $z/R$ . Predictions are with 0.5° blade pitch angle offset.

Table 2: Number of Sub-iterations (SI) and Residual Drop (RD) for High and Low Sub-iteration 3% $c$  cases

| Case    | OVERFLOW SI | OVERFLOW RD (OOM) | SAMCart SI | SAMCart RD (OOM) |
|---------|-------------|-------------------|------------|------------------|
| High SI | 100         | 0.97              | 27         | 2.0              |
| Low SI  | 60          | 0.74              | 18         | 1.3              |

(see Fig. 19). In the histogram, the experiment is colored in blue and the simulation is colored in red, where the first row is the 3% $c$  simulation and the second row is the 5% $c$  simulation. In the histogram plots, the peak demonstrates the max swirl and circulation value of most of the secondary vortices. Comparing 3% $c$  (first row) and 5% $c$  (second row) grid resolution, it appears that the 3% $c$  grid resolution simulation is qualitatively in much better agreement with the experiment regarding the distribution of the secondary vortices (for both circulation and maximum swirl velocity). However, both simulations agree with the experiment in that the predicted secondary vortices have a symmetric distribution of positive and negative circulation. In the next section, we will explain the mechanism causing the symmetric distribution of positive and negative circulation.

### Development of Secondary Vortices

Since the 3% $c$ , high sub-iterations case agrees best with the experiment, this case is used to elucidate the development of the secondary vortices. Figure 20 and 21 show the side and isometric view, respectively, of the z-vorticity (axial axis) contour plot at wake ages  $\Psi_w = 0.0^\circ, 30.0^\circ, 60.0^\circ$ , and  $90.0^\circ$ . In the contour plot, the red and blue contours show the sense of rotation of the vortices and vortex sheet, where counter-clockwise rotating is colored in red and clockwise rotating is colored in blue. The isometric view includes the Q-criterion isosurface to visualize the tip vortex. At early wake ages ( $\Psi_w \leq 30^\circ$ ), thin alternating counter-clockwise (colored red) and clockwise (colored blue) sheets of vortices are shed from the blade. From  $\Psi_w = 60^\circ - 90^\circ$ , the vortex sheets get entrained into the adjacent and preceding tip vortices, which stretches the vortex sheets and results in alternating counter-clockwise and clockwise rotating secondary vortices. This explains why there was a symmetric distribution of positive and negative secondary vortex circulation observed in the histogram plots in the previous section.

Figure 22 shows the early stages of evolution of the wake vortex system spanning from 5 to 16.5 revolutions. From 5 to 13 revolutions (first row), the tip vortices slowly move closer to one another. From 14.5 to 16.5 revolutions (second row), after the two tip vortices are close enough to each other, their corresponding secondary vortices that are wrapped around them collide (which are moving in opposite directions *between* the tip vortices), which causes tertiary vortices to be shed outside the mixing layer (circled in black).

Figure 23 shows the process for how the tip vortices pair and eventually decay alongside the secondary vortices. The figure spans from  $\Psi_w = 0^\circ$  to  $\Psi_w = 405^\circ$ . Each image going

from left to right is separated by  $45^\circ$ . For the discussion, the reader is referred to the two tip vortices within the black circles. At  $\Psi_w = 0^\circ$  (top left most figure), there is a gap between the secondary vortices that are wrapped around the tip vortices. At  $\Psi_w = 45^\circ$ , the secondary vortices coalesce. *Between* the tip vortices, the secondary vortices are rotating about the tip vortex axis in the opposite direction (shown by arrows) and therefore, the “S-shaped” mixing layer becomes elongated (see  $\Psi_w = 180^\circ$  and  $\Psi_w = 225^\circ$ ). From  $\Psi_w = 270^\circ$  to  $\Psi_w = 405^\circ$ , the tip vortices are pulled into one another as they pair and as this happens, the secondary vortices twist the primary vortex which results in the eventual decay of both the primary and secondary vortices.

## CONCLUSION

The development of secondary vortex structures in the wake of a two-bladed rotor was investigated by combining stereoscopic particle image velocimetry measurements in different measurement planes and high-fidelity simulations. Various numerical inputs including sub-iteration convergence, rotor thrust, blade pitch offset, and grid-resolution were varied to resolve vortex discrepancies between the experiment and simulation from a previous study done by the authors. The following conclusions have been drawn from this collaborative experimental and computational study:

1. A parametric study on near- and off-body solver sub-iteration convergence demonstrated that although the secondary vortex characteristics converged as the sub-iteration convergence of both solvers increased, a large discrepancy in the number of secondary vortices remained.
2. This discrepancy was investigated by varying the thrust, where it was found that the breakdown of the primary vortex is directly linked to the number of secondary vortices.
3. Dissimilarities in the blade pitch angle, which could not be avoided in the experiment, were modeled by intentionally using an offset in the blade pitch angle of the two blades. It was shown that as blade pitch angle offset increases, vortex pairing becomes more distinct. When vortex pairing occurred in both the experiment and simulation, the decay of secondary vortices in the experiment and simulation agreed best. However, an offset in the number of secondary vortices remained.
4. To better match the experimental resolution, the grid resolution was increased from 5% chord to 3% chord, and

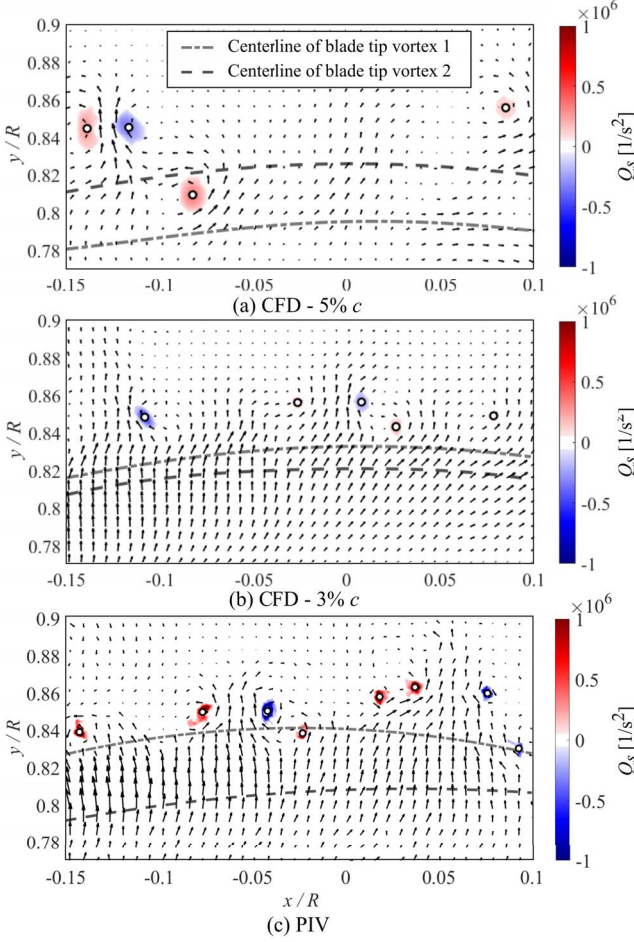


Figure 17: Comparison of the measured vs predicted (5% and 3% $c$ ) sample velocity fields at wake age of  $\Psi_w = 125^\circ$  taken at  $z/R = -0.4$ . The contours represent the signed  $Q$  values after applying the filtering scheme for secondary vortex detection. Predictions are with  $0.5^\circ$  blade pitch angle offset.

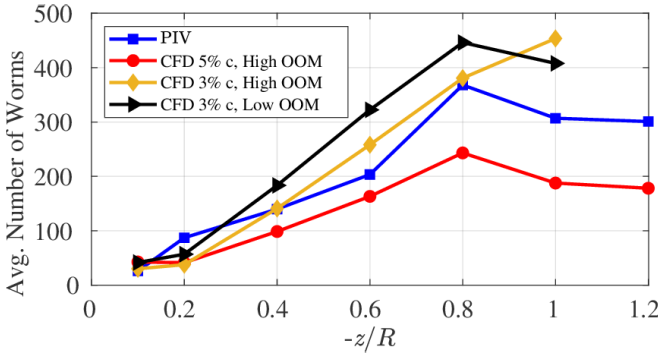


Figure 18: Figure shows variation in predicted secondary vortices as grid resolution and sub-iteration convergence varies. Predictions are with  $0.5^\circ$  blade pitch angle offset.

comparing the two grid resolution simulations, the finer mesh simulation agreed best with the measured primary and secondary vortex characteristics.

5. Investigation of the development process of the secondary vortices showed that thin alternating counter-

clockwise and clockwise sheets of vortices are shed from the blade. The vortex sheets get entrained into the adjacent and preceding tip vortices, which stretches the vortex sheets and results in alternating counter-clockwise and clockwise rotating secondary vortices. After the two tip vortices are close enough to each other, their corresponding secondary vortices that are wrapped around them collide, which causes tertiary vortices to be shed outside the mixing layer.

6. Secondary vortices impinging on structures below the rotor, which may have an impact on acoustic and vibration predictions, can be accurately predicted if the breakdown of the primary vortex is accurately captured and sufficient grid resolution/sub-iteration convergence is attained.

## ACKNOWLEDGMENTS

The experimental part of the study was conducted in the framework of the DLR project “URBAN-Rescue”. The authors thank M. Krebs, J. Braukmann, A. Kostek, F. Lößle, and R. Brinkema for their help in preparing and executing the rotor tests. The simulations presented in this paper is a product of the CREATE™-AV Element of the Computational Research and Engineering for Acquisition Tools and Environments (CREATE) Program sponsored by the U.S. Department of Defense HPC Modernization Program Office. Computational resources provided by the DoD High Performance Computing Modernization Office, Army S/AAA Roger Strawn, are greatly appreciated. Raw data were generated at the Department of Defense Supercomputing Resource Center (DSRC) large scale facility. Derived data supporting the findings of this study are available from the corresponding author upon reasonable request.

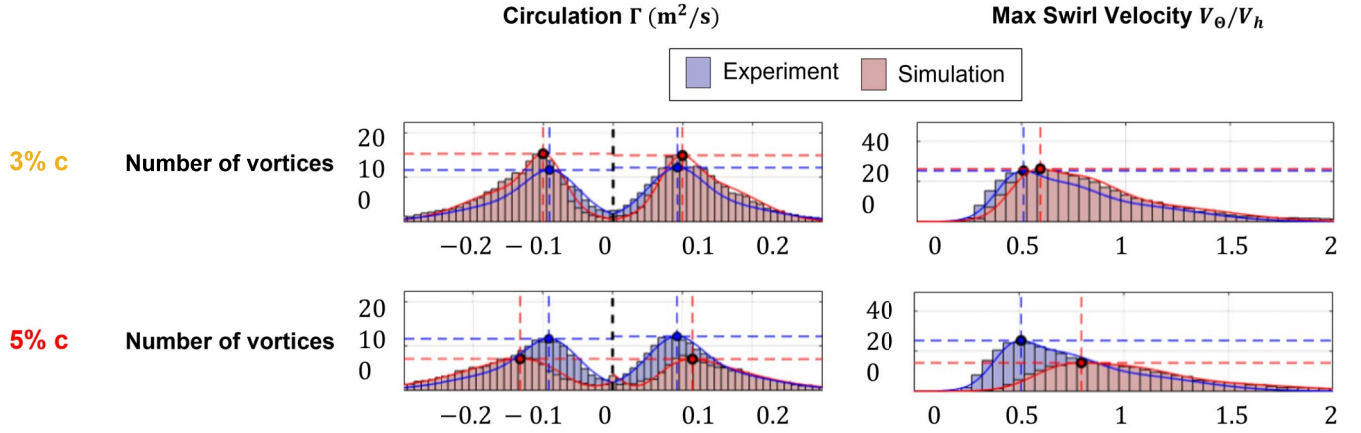


Figure 19: Effect of grid resolution on secondary vortex histograms of maximum swirl velocity  $V_{\theta,\max}/V_h$  (left column) and circulation  $\Gamma$  (right column) at  $z/R = -0.8$ .

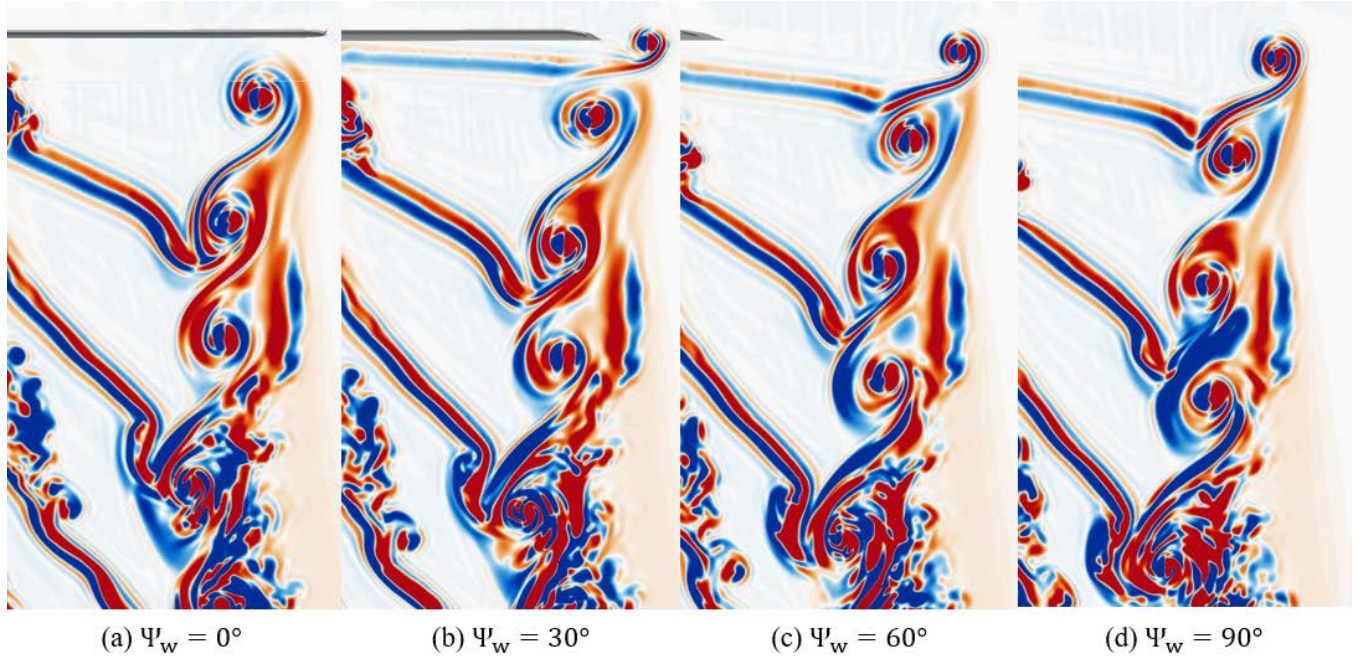
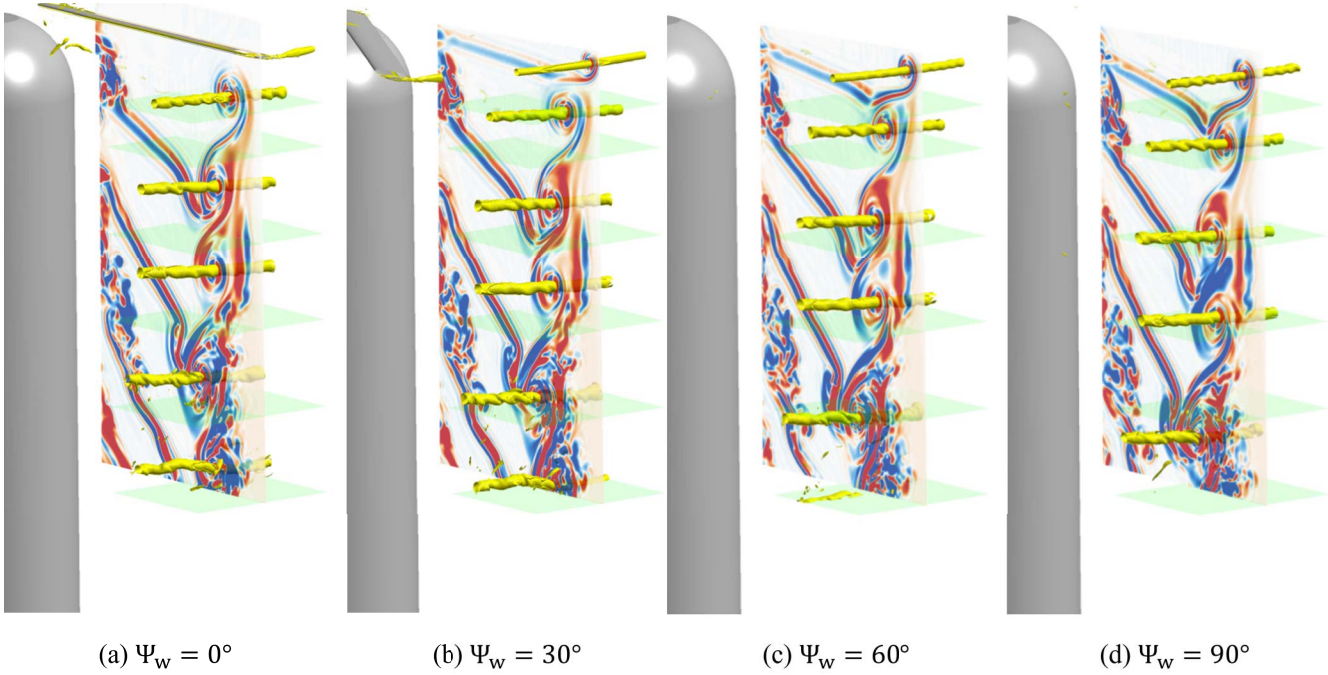


Figure 20: Z-vorticity contour plot at wake age of  $\Psi_w = 0.0^\circ, 30.0^\circ, 60.0^\circ$ , and  $90.0^\circ$ .



(a)  $\Psi_w = 0^\circ$

(b)  $\Psi_w = 30^\circ$

(c)  $\Psi_w = 60^\circ$

(d)  $\Psi_w = 90^\circ$

Figure 21: Z-vorticity contour plot superimposed with Q-criterion isosurfaces at wake age of  $\Psi_w = 0.0^\circ$ ,  $30.0^\circ$ ,  $60.0^\circ$ , and  $90.0^\circ$ .

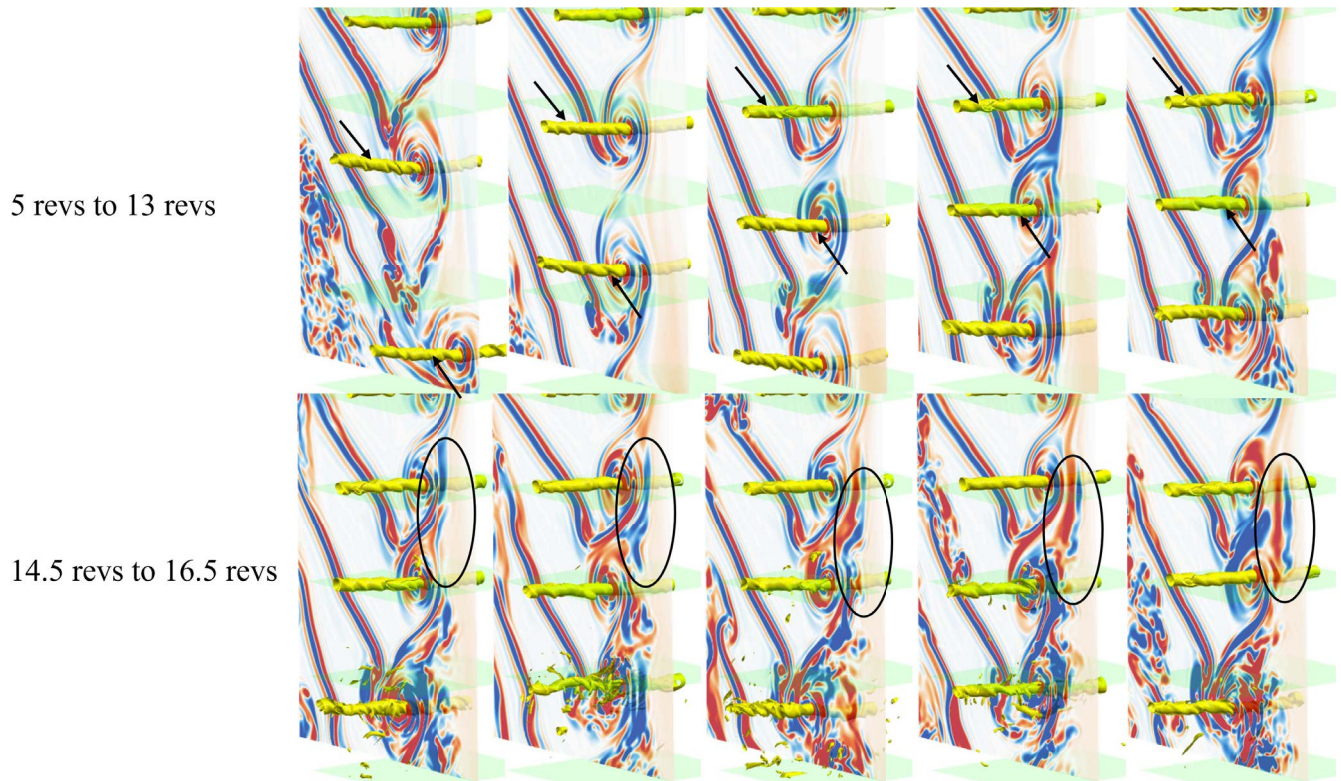


Figure 22: Visualization of the evolution of wake vortex system.

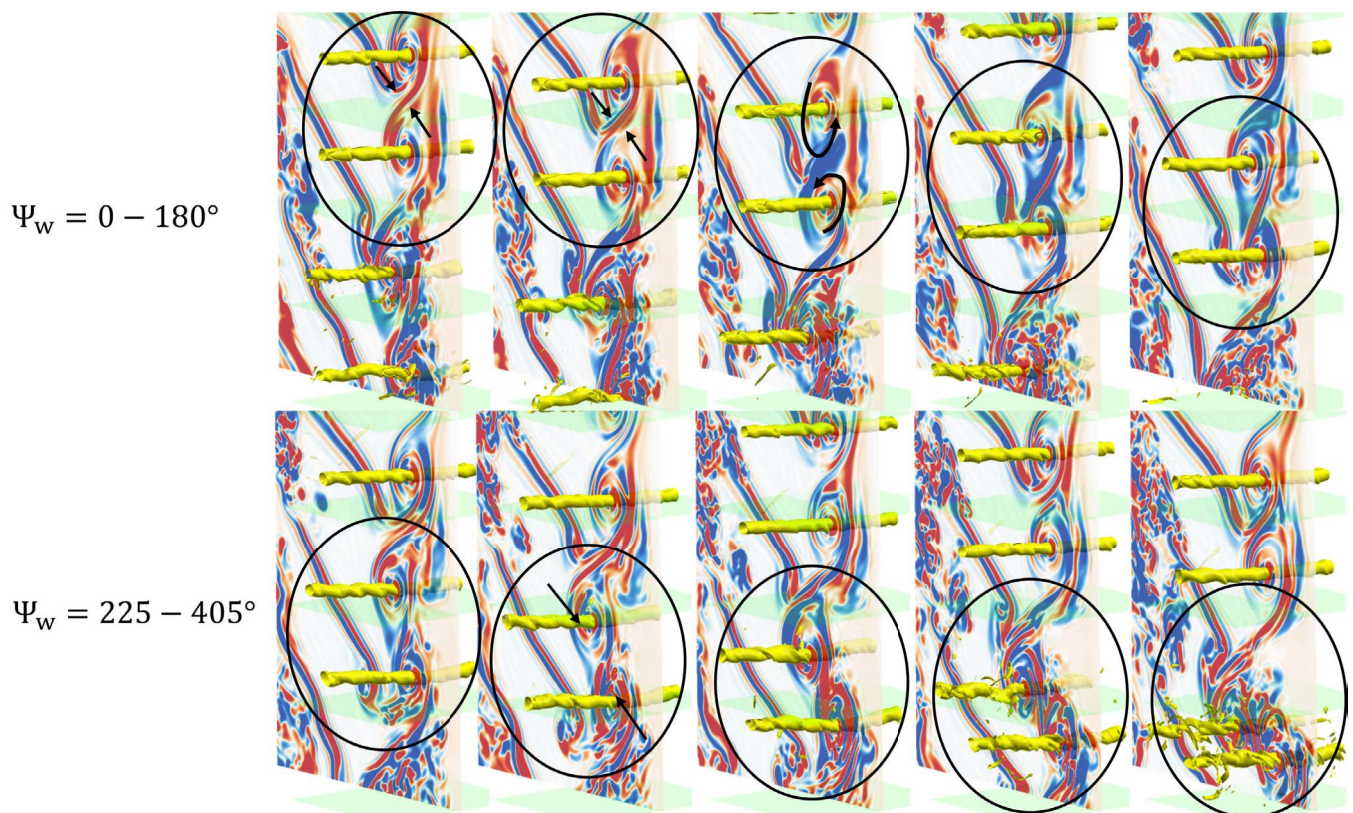


Figure 23: The evolution of tip vortex pairing.

## REFERENCES

1. Chaderjian, N., and Buning, P., "High Resolution Navier-Stokes Simulation of Rotor Wakes," AHS 67th Annual Forum, Virginia Beach, VA, May 3–5, 2011.
2. Jain, R., "A Comparison of CFD Hover Predictions for the Sikorsky S-76 Rotor," AIAA SciTech 54th Aerospace Sciences Meeting, San Diego, CA, January 4–8, 2016.
3. Abras, J., Hariharan, N. S., and Narducci, R. P., "Wake Breakdown of High-fidelity Simulations of a Rotor in Hover," Paper AIAA 2019-0593, AIAA Science and Technology Forum and Exposition, San Diego, CA, USA, January 7–11, 2019. DOI: 10.2514/6.2019-0593
4. Egolf, A., Hariharan, N. S., Narducci, R. P., and Reed, E., "AIAA Standardized Hover Simulation: Hover Performance Prediction Status and Outstanding Issues," Paper AIAA 2017-1429, 55th AIAA Aerospace Sciences Meeting, Grapevine, TX, USA, January 9–13, 2017. DOI: 10.2514/6.2017-1429
5. Hariharan, N., Abras, J., and Narducci, R., "An Overview of Wake Breakdown in High-Fidelity Simulations of Rotor-in-Hover," Vertical Flight Society 75th Annual Forum, Virtual, October 5–8, 2020.
6. Wolf, C. C., Schwarz, C., Kaufmann, K., Gardner, A. D., Michaelis, D., Bosbach, J., Schanz, D., and Schröder, A., "Experimental study of secondary vortex structures in a rotor wake," *Experiments in Fluids*, Vol. 60, (175), 2019. DOI: 10.1007/s00348-019-2807-1
7. Bodling, A., and Potsdam, M., "Numerical Investigation of Secondary Vortex Structures in a Rotor Wake," *Journal of the American Helicopter Society*, Vol. 67, (4), October 2022, pp. 1–18. DOI: doi: 10.4050/JAHS.67.042007
8. Schwarz, C., Bodling, A., Wolf, C., Brinkema, R., Potsdam, M., and Gardner, A., "Development of secondary vortex structures in rotor wakes," *Experiments in Fluids*, Vol. 63, (1), 2022. DOI: 10.1007/s00348-021-03348-8
9. Wissink, A. M., Dylan, J., Jayaraman, B., Roget, B., Lakshminarayan, V. K., Sitaraman, J., Bauer, A. C., Forsythe, J., and Trigg, R. D., "New Capabilities in CREATE-AV Helios Version 11," AIAA Science and Technology Forum and Exposition, Virtual Event, January 11–15 & 19–21, 2021. DOI: 10.2514/6.2021-0235
10. Sitaraman, J., Floros, M., Wissink, A., and Potsdam, M., "Parallel domain connectivity algorithm for unsteady flow computations using overlapping and adaptive grids," *Journal of Computational Physics*, Vol. 229, (12), 2010, pp. 4703–4723. DOI: 10.1016/j.jcp.2010.03.008
11. Biedron, R. T., Carlson, J., Derlaga, J. M., Gnoffo, P. A., Hammond, D. P., Jones, W. T., Kleb, B., Lee-Rausch, E. M., Nielsen, E., Park, M., Rumsey, C., Thomas, J., Thompson, K. B., and Wood, W., "FUN3D Manual: 13.5," NASA TM 220271, April 2019.
12. Allmaras, S. R., Johnson, F., and Spalart, P. R., "Modifications and Clarifications for the Implementation of the Spalart-Allmaras Turbulence Model," Seventh International Conference on Computational Fluid Dynamics, Big Island, Hawaii, July 2012.
13. Dacles-Mariani, J., Kwak, D., and Zilliac, G., "On Numerical Errors and Turbulence Modeling in Tip Vortex Flow Prediction," *International Journal for Numerical Methods in Fluids*, Vol. 30, (1), 1999, pp. 65–82. DOI: 10.1002/(SICI)1097-0363
14. Spalart, P. R., Deck, S., Shur, M. L., Squires, K., Strelets, M. K., and Travin, A., "A New Version of Detached-eddy Simulation, Resistant to Ambiguous Grid Densities," *Theoretical and Computational Fluid Dynamics*, Vol. 20, 2006, pp. 181. DOI: 10.1007/s00162-006-0015-0
15. Buning, P., and Nichols, R., "User's Manual for OVERFLOW 2.3," <https://overflow.larc.nasa.gov/home/users-manual-for-overflow-2-3/>, January 2023.
16. Jespersen, D. C., Pulliam, T. H., and Buning, P., "Recent enhancements to OVERFLOW," Paper AIAA 97-0644, 35th AIAA Aerospace Sciences Meeting, Reno, NV, January 6–9, 1997.

17. Shur, M., Stelets, M., Travin, A., and Spalart, P., "Turbulence Modeling in Rotating and Curved Channels: Assessing the Spalart-Shur Correction," *AIAA Journal*, Vol. 38, (5), 2000, pp. 784–792. DOI: 10.2514/2.1058
18. Wissink, A. M., Sitaraman, J., Jayaraman, B., Roget, B., Lakshminarayan, V. K., Potsdam, M. A., Jain, R., Bauer, A., and Strawn, R., "Recent Advancements in the Helios Rotorcraft Simulation Code," Paper AIAA 2016-0563, 54th AIAA Aerospace Sciences Meeting, 2016.
19. Leffell, J. I., Sitaraman, J., Lakshminarayan, V. K., and Wissink, A. M., "Towards Efficient Parallel-in-Time Simulation of Periodic Flows," 54th AIAA Aerospace Sciences Meeting, 2016.
20. Chen, Q., Zhong, Q., Qi, M., and Wang, X., "Comparison of vortex identification criteria for planar velocity fields in wall turbulence," *Physics of Fluids*, Vol. 27, (085101), 2015. DOI: 10.1063/1.4927647